

## Radiation-enhanced diffusion under conditions of non-steady state and non-homogeneity of excess defects

This article has been downloaded from IOPscience. Please scroll down to see the full text article.

2004 J. Phys.: Condens. Matter 16 R581

(<http://iopscience.iop.org/0953-8984/16/18/R02>)

[View the table of contents for this issue](#), or go to the [journal homepage](#) for more

Download details:

IP Address: 129.252.86.83

The article was downloaded on 27/05/2010 at 14:33

Please note that [terms and conditions apply](#).

## TOPICAL REVIEW

# Radiation-enhanced diffusion under conditions of non-steady state and non-homogeneity of excess defects

Ming Lu<sup>1</sup>, Corina Lupu<sup>2</sup> and J Wayne Rabalais<sup>2,3</sup>

<sup>1</sup> Department of Optical Science and Engineering, Fudan University, Shanghai 200433, People's Republic of China

<sup>2</sup> Department of Chemistry, University of Houston, Houston, TX 77204-5003, USA

E-mail: rabalais@uh.edu

Received 28 January 2004

Published 23 April 2004

Online at [stacks.iop.org/JPhysCM/16/R581](http://stacks.iop.org/JPhysCM/16/R581)

DOI: 10.1088/0953-8984/16/18/R02

## Abstract

Radiation-enhanced diffusion, or RED, has been conventionally studied under the conditions of steady state and homogeneous background of excess defects. Hence MeV ion irradiation and diffusion annealing were conducted simultaneously and the temporal and spatial dependences of the diffusing parameters were ignored. This review covers a new type of RED, i.e. non-steady-state radiation-enhanced diffusion or NSRED. The sequence of steps in NSRED are (i) keV ion irradiation of the substrate to create defects, (ii) evaporation of the diffusing materials onto the surface, followed by (iii) diffusion annealing. Using such a sequence, the diffusion region directly overlaps with the central region of the ion implantation profile. Ti diffusion in ion pre-irradiated MgO(100) was selected as a model diffusion system, ions of Ar<sup>+</sup>, Ne<sup>+</sup>, Kr<sup>+</sup>, Cl<sup>+</sup> and Cr<sup>+</sup> were used for irradiation and diffusion was conducted in an inert atmosphere. Secondary ion mass spectroscopy (SIMS) was used to depth-profile the diffusing materials. A phenomenological model based on the concept of depth-dependent diffusion coefficients was developed to quantify the NSRED results. Monte Carlo (TRIM) simulations were used to model the implantation. Compared to conventional RED, vacancy clusters, rather than excess mono-vacancies, are the dominant contributors to NSRED, resulting in two unique observations. The first is a post-irradiation annealing effect, i.e. annealing a pre-irradiated substrate enhances the subsequent diffusion. This is due to the key roles of vacancy clusters in the diffusion enhancement. The second is a chemical effect, i.e. the enhanced diffusion does not only depend on the ballistic behaviours of the irradiating ions, as in conventional RED, but on the chemical properties of the ions as well. This effect is consistent with a modified vacancy-clustering model. The

<sup>3</sup> Author to whom any correspondence should be addressed.

results indicate that NSRED is a promising technique for modification of the optical and mechanical properties of oxides through manipulation of doping ion diffusion behaviours in a well-controlled manner.

## Contents

1. Introduction	582
2. Experimental details	583
3. Results and discussion	584
3.1. Observation and quantification of NSRED	584
3.2. Nature of excess defects for NSRED	587
3.3. Post-irradiation annealing effect on NSRED	589
3.4. Chemical effect of NSRED	595
3.5. Sensitivity of NSRED to defects and impurities	599
4. Conclusions and outlook	600
Acknowledgments	601
References	601

### 1. Introduction

Cation diffusion in oxides is important from the viewpoints of both fundamental research and applications to defect-related studies, fusing ceramics and modification of mechanical and optical properties of solids (Sangster and Stoneham 1994, Ohkubo *et al* 1986, Specht *et al* 1992, McHargue and Snyder 1983, Yang and Flynn 1994, Fielitz *et al* 1997, Demaree *et al* 1997, Bigarre *et al* 1997). It has been known for a long time that energetic ion irradiation of crystalline solids produces excess defects that can facilitate atom diffusion. This is called radiation-enhanced diffusion, or RED (Diens and Damask 1958, Sizmann 1978, Macht and Naundorf 1982, Mueller *et al* 1988, Lee *et al* 1994, Van Sambeek *et al* 1998, Wei *et al* 1999). Theoretical models for RED resulting in a series of rate equations were proposed by Diens and Damask (1958) and Sizmann (1978). These coupled equations yielded reliable physical outputs such as vacancy production rates Wei *et al* (1999) and diffusion coefficients (Van Sambeek *et al* 1998) when the conditions of steady state and homogeneous background of excess defects were met. The temporal and spatial evolutions of the excess defects were not included. For verification and application of these proposed models, RED experiments have conventionally been conducted in such a manner that ion irradiation and diffusion annealing were performed simultaneously in order to achieve a steady state condition for the concentration of defects. In most of the studies, MeV ion beams with long projectile ranges were used for irradiation so that diffusion was able to proceed far away from the central region of the implantation profile and, hence, in a homogeneous background of excess defects. Furthermore, in order to avoid sputtering of diffusing materials during diffusion, the diffusing species were buried inside the substrate by means of molecular beam epitaxy (MBE) prior to MeV implantation. Such a diffusion–irradiation procedure and sample geometry requirement have limited the broader applications of RED.

For flexibility in future applications, we have explored a different type of RED (Weiss *et al* 2000, Lu *et al* 2001, 2002a, 2002b, 2002c, 2002d, 2002e, 2003) consisting of the sequence (1) ion irradiation of the substrate to produce excess defects, (2) evaporation of diffusing species onto the surface of the substrate and (3) diffusion annealing. The more commonly available keV

ion beam sources were used for ion irradiation. This new type of non-steady-state radiation-enhanced diffusion (NSRED) was found to possess different diffusion behaviours from the conventional type. NSRED proceeds in an environment of inhomogeneously distributed excess defects. In the diffusion-irradiation procedure, NSRED is similar to transient-enhanced diffusion (TED), a phenomenon encountered in the Si microelectronics industry (Cowen *et al* 1990, Eaglesham *et al* 1994, Rafferty *et al* 1996, Wen *et al* 1996, Moller *et al* 1998, Shao *et al* 2000). However, the two enhanced diffusion processes are different in three aspects:

- (1) In TED the diffusants are the implants themselves and, hence, the diffusing species are located inside the substrate before diffusion. For NSRED, the diffusants can be any desired species and they are initially placed on the surface of the substrate.
- (2) The ion energy used in TED is in the range of tens of keV to MeV, while that for NSRED is 1–10 keV.
- (3) The motivation of TED studies is to suppress the enhanced diffusion, while NSRED was developed for manipulating cationic diffusion behaviours such as diffusion ranges and diffusant depth profiles in the substrate. By manipulating diffusion in a controlled manner, it is possible to tune the optical and mechanical properties of implanted substrate materials (e.g. Lu *et al* 2001).

In this work, Ti diffusion in ion-irradiated MgO(100) was selected as a model system for NSRED. MgO is a basic material for ceramic fabrication and its bulk and surface properties have been thoroughly investigated (e.g. Yang and Flynn 1994, Perry and Merrill 1997). Our objective in initiating this diffusion work was aimed at modification of the optical and mechanical properties of oxides through controlled cationic doping. Mass- and energy-selected ion beams of Ar<sup>+</sup>, Ne<sup>+</sup>, Kr<sup>+</sup>, Cl<sup>+</sup> and Cr<sup>+</sup> were used to create excess defects in MgO(100). Ti was evaporated onto the ion pre-irradiated MgO surface and the diffusion was subsequently induced by thermal annealing. Diffusion penetration profiles were obtained by using secondary ion mass spectroscopy (SIMS) depth profiling techniques. TRIM classical ion trajectory simulations (Ziegler 1996) were used to assist in clarifying the NSRED mechanism.

The focus of this review is on three topics: (1) the observation of NSRED and its quantification, (2) the post-irradiation annealing effect and (3) the chemical effect in NSRED. The latter two effects are unique to NSRED. Our proposed divacancy creation model and modified vacancy-clustering model explain the latter two effects, respectively, as will be shown in sections 3.3 and 3.4.

## 2. Experimental details

MgO(100) single crystals were obtained from MTI Inc. (Richmond, CA). They were supersonically cleaned with acetone, followed by annealing in an oxygen atmosphere (1 atm, 1100 °C, 2 h) so as to minimize the number of intrinsic defects in MgO and project the effects due to the excess defects produced by ion irradiation (Moya *et al* 1998). Before ion irradiation and evaporation, the MgO(100) was further annealed at 1000 °C for 5 min in the main ultra-high vacuum (UHV) chamber of the mass-selected, low energy ion beam (LEIB) instrument of the University of Houston (Albayati *et al* 1994) in order to achieve an atomically flat surface (Perry and Merrill 1997). Mass-selected ion beams were employed for irradiation at the normal incident angle with ion fluxes of  $\sim 1 \mu\text{A cm}^{-2}$ . The ion energy ranged from 1.7 to 9.5 keV and the ion dose was between  $5-50 \times 10^{15} \text{ cm}^{-2}$ . Most of the work used 7 keV ion beams with a dose of  $5 \times 10^{15} \text{ cm}^{-2}$ . Ten monolayers of Ti were evaporated onto the MgO surface for all of the samples in this work. The evaporation was performed by using a water-cooled UHV evaporator (Omicron, Model EFM3) at a rate of  $0.4 \text{ ML min}^{-1}$  that had been calibrated with a

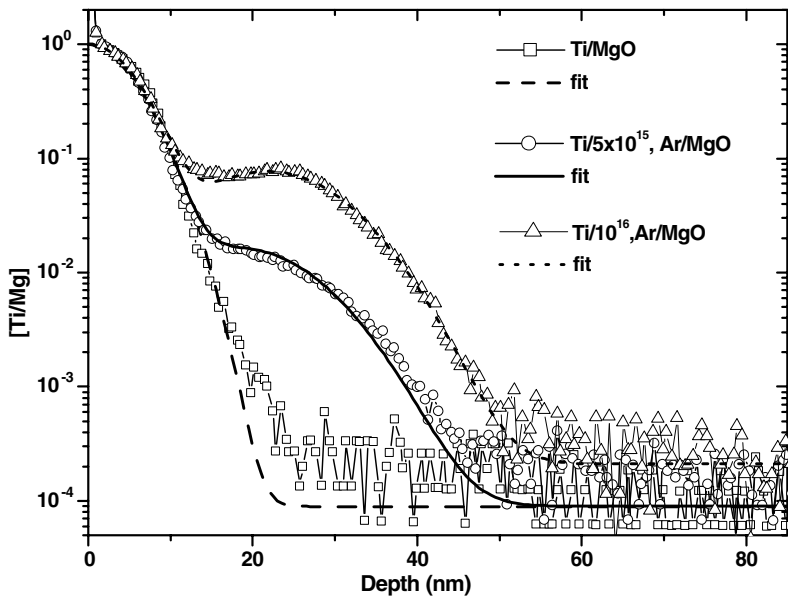


**Figure 1.** SIMS depth profiles of the intensity ratio [Ti/Mg] for Ti evaporated on MgO (Ti/MgO) and Ti evaporated on MgO that had been pre-irradiated by 7 keV Ar<sup>+</sup> for doses of  $5 \times 10^{15}$  ions cm<sup>-2</sup> (Ti/5  $\times 10^{15}$ , Ar/MgO) and  $1 \times 10^{16}$  ions cm<sup>-2</sup> (Ti/10<sup>16</sup>, Ar/MgO) after diffusion at 1000 °C for 6 min. The data fitting was performed by using the model in section 3.1.

microbalance (Maxtek, Inc., Model TM-350/340). The pressure remained below  $2 \times 10^{-9}$  mbar during evaporation. The samples were briefly exposed to air prior to diffusion. Diffusion was carried out at 1000 °C in a tube furnace in 1 atm of Ar. In the diffusion procedure, the sample temperature was ramped up from room temperature to 1000 °C in  $\sim 5$  s and, after the desired diffusion time ( $\geq 6$  min), the diffusion was quenched within 20 s. The nearly abrupt changes of temperature allowed a precise determination of diffusion coefficients. In order to explore the post-irradiation annealing effect, or briefly, post-annealing effect, after 7 keV Ar<sup>+</sup> irradiation, the samples were post-annealed in UHV at various temperatures ( $T_{pa} = 800, 900, 1000$  and 1100 °C) for various times ( $\tau = 5, 10$  and 20 min). For the investigation of chemical effects, ion beams of Cl<sup>+</sup> and Cr<sup>+</sup> were used for comparison to Ar<sup>+</sup>. The ballistic behaviours of these three ions are similar; however, their chemical properties are different.

SIMS depth profiles were recorded on a PHI Model 6600 instrument. Cs<sup>+</sup> primary ion beams of 20 nA at 5 keV directed at 60° to the surface normal were used for sputter depth profiling. The beams were rastered over a  $300 \times 300 \mu\text{m}^2$  area and the analysis was gated to 60% of the rastered area. A low energy electron beam was used to control sample charging. The sputtering rate was calibrated by measuring the crater depths using a stylus profilometer. A linear time to depth relation was assumed. Since the mass of <sup>48</sup>Ti coincides with that of <sup>24</sup>Mg<sub>2</sub>, the less abundant <sup>46</sup>Ti isotope was used for depth profiling.

### 3. Results and discussion

#### 3.1. Observation and quantification of NSRED

Figure 1 shows the SIMS depth profiles of Ti for three different samples after diffusion at 1000 °C for 6 min. The conditions are: (Ti/MgO)—Ti evaporated on MgO; (Ti/10<sup>15</sup>, Ar/MgO) and (Ti/10<sup>16</sup>, Ar/MgO)—Ti evaporated on MgO that had been pre-irradiated by

7 keV Ar<sup>+</sup> for doses of  $5 \times 10^{15}$  and  $1 \times 10^{16}$  ions cm<sup>-2</sup>, respectively. The ordinate is the SIMS intensity ratio of <sup>46</sup>Ti divided by <sup>24</sup>Mg, i.e. [Ti/Mg]. For convenience of data analysis, [Ti/Mg] values were normalized so that the value at the surface is unity. This normalization has been performed throughout the work. Enhanced diffusion is observed for both pre-irradiated samples, which is characterized by a convex profile beginning at a depth  $>\sim 13$  nm. The convex part is more pronounced at larger doses. The convex profiles have been observed for Ti diffusion in MgO pre-irradiated with either inert or reactive ions and for various doses, energies, momenta and penetration ranges. This shows that enhanced diffusion, or NSRED, exists for the adopted diffusion–irradiation procedure and sample geometry. The diffusion depth profile of NSRED differs from that of the conventional type where an overall broadening of the depth profile has been found and the profile remains a Gaussian-like form.

The implantation range of the 7 keV Ar<sup>+</sup> is critical for Ti diffusion. Due to the mass overlap of <sup>40</sup>Ar with the substrate <sup>40</sup>(MgO), 7 keV <sup>48</sup>Ti<sup>+</sup> was used to determine the implantation range. The mass of Ti<sup>+</sup> is close to that of Ar<sup>+</sup> and so are their ballistic behaviours, as shown by TRIM simulations. The resulting <sup>48</sup>Ti depth profile was found to peak at a depth of  $\sim 23$  nm in a Gaussian-like shape with the full width at half-maximum (FWHM) of  $\sim 40$  nm. The observed ion range is three times larger than that determined from TRIM simulations. Considering that single-crystalline wafers of MgO were used in this work, while TRIM treats amorphous targets, this difference can be attributed to the deeper penetration of ions by channeling into the ordered regions of the crystal and to defect migration during ion irradiation (Canut *et al* 1991). The diffusion range then overlaps heavily with the central region of the profile of ion implantation as seen in figure 1, hence the diffusion proceeds in an inhomogeneous background of defects. Based on this conclusion, NSRED was modelled as follows.

A solid state diffusion process can be described by Fick's law (Borg and Diens 1988, Mrowec 1980) as

$$\frac{\partial C}{\partial t} = \frac{\partial}{\partial x} \left( D \frac{\partial C}{\partial x} \right) \quad (1)$$

where  $C$  is the concentration of diffusing atoms,  $t$  is the diffusion time,  $x$  is the distance perpendicular to the surface (depth) and  $D$  is the diffusion coefficient. Since the defects are depth-dependent in the range of diffusion for the pre-irradiated sample, the parameter  $D$  is also depth-dependent. The excess defects induced by ion pre-irradiation have Gaussian distributions as shown by TRIM simulations. Since  $D$  is proportional to the number of defects, mainly vacancies and interstitials, it is appropriate to assume that the diffusion coefficient  $D$  versus depth  $x$  follows a Gaussian expression:

$$D = D_0 + D_1 \exp(-(x - L)^2/\lambda^2). \quad (2)$$

Here  $D_0$  is the diffusion coefficient for MgO before irradiation and correlates with the original uniform distribution of defects. The second term reflects the RED effect and correlates with the excess defect distribution,  $D_1$  is a diffusion constant,  $L$  is the peak location of the Gaussian and  $\lambda^2$  is its variance. The latter three parameters are diffusion-time-dependent (that is why the NSRED is so named). This was found from our experiments to be especially true for  $D_1$  (Lu *et al* 2002a). Considering that the numbers of vacancies (Zhou and Manasreh 2002) and interstitial clusters (Moller *et al* 1998) change with annealing time in an exponential decay manner,  $D_1$  in equation (2) can then be replaced with

$$D_1 = D_{10} \exp(-\kappa t), \quad (3)$$

where  $\kappa$  is a rate constant and  $D_{10}$  is a constant reflecting the peak value of the initial excess defect distribution. After inserting equations (2) and (3) into (1), numerical solutions (Pang 1997) of equation (1) would yield the relationship of the concentration of diffusant ( $C$ ) and

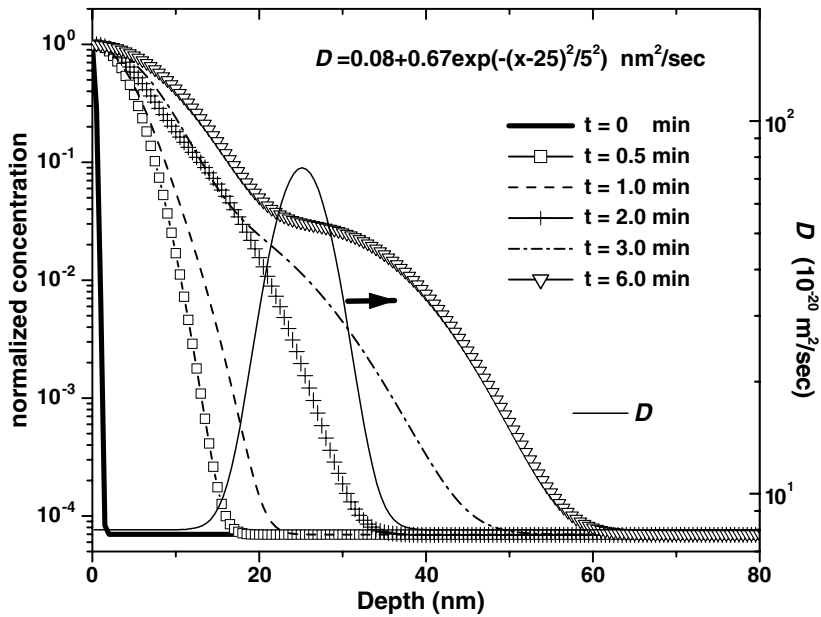


**Figure 2.** Time evolution of the normalized concentration versus depth (left ordinate) obtained by solving equation (1) based on a specific depth-dependent diffusion coefficient (right ordinate).

**Table 1.** Fitting parameters for Ti diffusion in MgO(100) pre-irradiated with 7 keV Ar<sup>+</sup>.

	Ti/MgO	Ti/Ar/MgO	Ti/10 <sup>16</sup> , Ar/MgO
$D_0$ (10 <sup>-20</sup> m <sup>2</sup> s <sup>-1</sup> )	2.9	2.9	2.9
$D_{10}$ (10 <sup>-18</sup> m <sup>2</sup> s <sup>-1</sup> )	0.0	1.5	6.4
$L$ (nm)	—	19.0	23.5
$\lambda^2$ (nm <sup>2</sup> )	—	22.0	25.0
$\Sigma$ (nm <sup>3</sup> s <sup>-1</sup> )	0.0	12.2	56.3
$\bar{\Sigma}$ (nm <sup>3</sup> s <sup>-1</sup> )	0.0	8.3	38.1

the depth ( $x$ ). For simulation of the NSRED process,  $C-x$  curves for various diffusion times were calculated from equation (1) and are represented in figure 2. They are based on an assumed  $D$  value in equation (2) in order to simulate the process of NSRED. Here  $D_1$  was taken as a constant, independent of the diffusion time. This assumption does not change the general conclusion drawn from the simulation results, i.e. where the number of diffusing atoms crossing the excess defect region and represented by the Gaussian part of  $D$  becomes large enough (for  $t > 1.0$  min in this case), the concentration profile features a convex structure, indicative of enhanced diffusion (figure 1). Therefore, by adjusting parameters such as  $D_0$ ,  $D_{10}$ ,  $L$  and  $\lambda^2$  within reasonable ranges so as to best fit the experimental data with our model, quantification of NSRED can be realized. In order to assess the degree of enhanced diffusion, a figure of merit which reflects the amount of excess defects for NSRED was introduced as

$$\Sigma = \int_0^{\infty} D_{10} \exp(-(x - L)^2/\lambda^2) dx. \quad (4)$$

The curves in figure 1 correspond to the fitting curves that were obtained after application of the above model. The fitting parameters are listed in table 1. For larger irradiation doses, the diffusion was more enhanced, which was quantified through the values of  $\Sigma$  (table 1). The

value of  $\kappa = 0.065 \text{ min}^{-1}$  corresponds to the diffusion annealing temperature of  $1000^\circ\text{C}$ . Since the diffusion temperature and time were identical for the three samples, a diffusion-temperature-independent  $D_1$  was also considered. This implies an average defect density distribution in time, so the resulting  $\Sigma$  was termed as  $\bar{\Sigma}$ . Table 1 shows that the ratio of  $\bar{\Sigma}$  of  $(\text{Ti}/10^{16}, \text{Ar}/\text{MgO})$  to that of  $(\text{Ti}/5 \times 10^{15} \text{ Ar}/\text{MgO})$  is 4.6, i.e. the same as that of  $\Sigma$ . Hence the  $\bar{\Sigma}$  reflects the degree of RED as well as  $\Sigma$ . Calculation times could be shortened by using  $\bar{\Sigma}$  to compare the degree of NSRED. However, it should be noted that this approximation is appropriate only if the samples for comparison were annealed at the same diffusion temperature and for the same time.

### 3.2. Nature of excess defects for NSRED

As stated in section 1, NSRED resembles the transient-enhanced diffusion (TED) process where the implanted dopants diffuse abnormally in Si during the post-implantation annealing step. It is this type of procedure that results in both enhanced diffusions producing a non-steady state concentration of excess defects. The difference between NSRED and TED lies in the initial location of diffusing materials—one is evaporated onto the surface (NSRED) and the other is implanted into the material (TED). This should not alter the nature of defects responsible for diffusion enhancements. Hence, the existing TED interpretations are possibly transferable to understand the mechanism of NSRED. It is known that the freely mobile defects (mainly mono-interstitials and mono-vacancies) induced by ion pre-irradiation are annihilated very quickly due to recombination at elevated temperatures. For instance, Si mono-interstitials and vacancies induced by 5 keV  $\text{Xe}^+$  irradiation of Si disappear within  $10^{-7} \text{ s}$  at an annealing temperature of  $350^\circ\text{C}$ , leaving only defect clusters inside the Si substrate (Bedrossian *et al* 1997). It has been established that it is the Si mono-interstitials that enhance dopant boron diffusion via an interstitial-like mechanism (Cowen *et al* 1990, Eaglesham *et al* 1994, Borg and Diens 1988). It is believed that the excess Si mono-interstitials come from thermal dissociation of rod-like  $\text{Si}\{311\}$  clusters formed by ion implantation (Cowen *et al* 1990, Eaglesham *et al* 1994, Rafferty *et al* 1996, Wen *et al* 1996, Moller *et al* 1998, Shao *et al* 2000). The  $\text{Si}\{311\}$  clusters act as a source of Si mono-interstitials, providing these freely mobile defects that are responsible for the observed enhanced dopant diffusion. For Ti diffusion in  $\text{MgO}$ , it is widely accepted that diffusion follows a vacancy mechanism (Yang and Flynn 1994, Van Sambeek *et al* 1998, Mrowec 1980, Borg and Diens 1988), that is,  $\text{Ti}^{n+}$  species migrate on the Mg sublattice via Mg mono-vacancies. By reference to the case of TED, it is likely that these freely mobile vacancies are generated by the thermal dissociation of some extended vacancy defects such as vacancy clusters induced by ion pre-irradiation. This interpretation is plausible since ion irradiation can produce vacancy clusters near the centre of collision cascades (Kapinos and Platonov 1985a, 1985b, 1987, Pramanik and Seidman 1983, Diaz de la Rubia *et al* 1990). Van Sambeek *et al* (1998) in their work on RED in  $\text{MgO}$ , emphasized the role played by the Mg vacancy clusters in enhancing cation diffusion.

Figure 3 represents the degree of NSRED (average  $\Sigma$  or  $\bar{\Sigma}$ ) and  $D_0$  versus irradiation dose. The conditions used are 7 keV  $\text{Ar}^+$  beam,  $\text{Ar}^+$  doses  $0, 5 \times 10^{15}, 10^{16}, 3 \times 10^{16}$ , and  $5 \times 10^{16} \text{ ions cm}^{-2}$ , and diffusion was carried out at  $1000^\circ\text{C}$  for 6 min ( $\bar{\Sigma}$  is adopted for brevity). It can be seen that  $D_0$  remains constant, indicating that the original vacancy distributions are not changed after ion irradiation. This is also reflected in figure 1, where the depth profiles of the pre-irradiated samples nearly coincide in the range of 0–13 nm with that for  $\text{Ti}/\text{MgO}$ . This observation supports the idea that the nature of the vacancies responsible for NSRED is different and that mono-vacancies induced by ion pre-irradiation are not responsible for the observed enhanced diffusion. Figure 3 demonstrates that  $\bar{\Sigma}$  increases rapidly with  $\text{Ar}^+$  dose

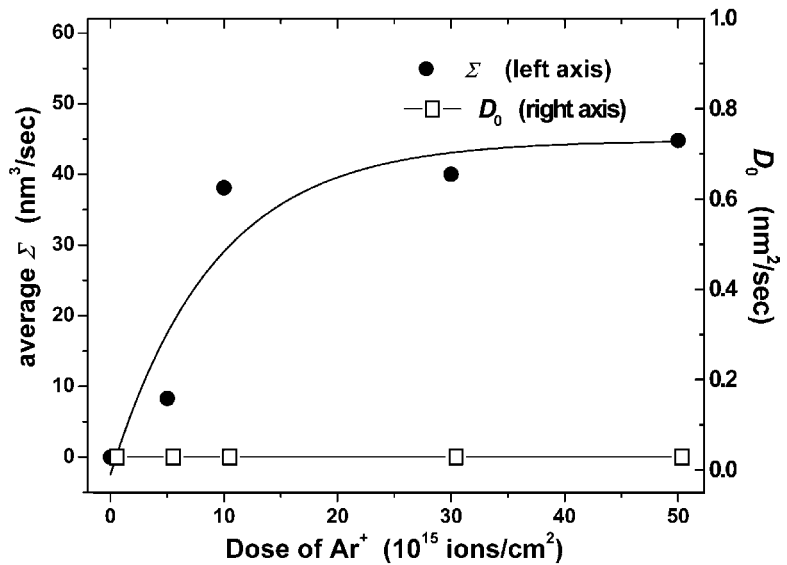


**Figure 3.** Average  $\Sigma$  and bulk diffusion coefficient  $D_0$  after  $\text{Ar}^+$  pre-irradiation versus  $\text{Ar}^+$  dose. The curves were drawn to guide the eye.

up to  $\sim 10^{16}$  ions  $\text{cm}^{-2}$ , then it approaches a saturation value. This behaviour is as expected. During irradiation, the surface region is continuously being removed by sputtering, resulting in its erosion. Therefore the number of defects created by ion irradiation do not increase indefinitely with irradiation time, because a steady state situation is achieved in which excess defects are produced in the substrate due to irradiation while the defects near the surface are sputtered. These two counteracting processes reach a steady state situation after a sufficiently long irradiation time or dose and the defect distribution inside the  $\text{MgO}$  tends to become constant (see Lu *et al* 2002b).

In order to gain more insight into the mechanism of NSRED, the degree of NSRED as a function of irradiating ion mass was explored. Inert ion beams of  $^{20}\text{Ne}^+$ ,  $^{40}\text{Ar}^+$  and  $^{84}\text{Kr}^+$  were selected with irradiation doses of  $5 \times 10^{15}$  ions  $\text{cm}^{-2}$ , diffusion temperature  $1000^\circ\text{C}$  and diffusion time 6 min.  $\bar{\Sigma}$  was used for evaluating the degree of NSRED. Figure 4 shows the relationship of  $\bar{\Sigma}$  and ion mass for ion energies of 7 keV for the three ions. The values of the vacancy production rates,  $V$ , generated by TRIM simulations are also given. Although amorphous targets are assumed in TRIM, it is expected that the results can still provide the correct trends when comparing different ion/target systems if only ballistic radiation effects are considered, which is true for this part of the work since chemically inert ions were used. Figure 5 shows plots of  $\bar{\Sigma}$  versus mass number for  $\text{Ne}^+$ ,  $\text{Ar}^+$  and  $\text{Kr}^+$  with energies 4.4, 7.0 and 9.5 keV, respectively, along with the values of  $V$ . These energies were chosen so that the penetration ranges for the three ions were identical (7.1 nm) as predicted by TRIM calculations. An additional set of data for  $\bar{\Sigma}$  and  $V$  versus mass number are presented in figure 6 for ion energies of 7.0, 3.5 and 1.7 keV for  $\text{Ne}^+$ ,  $\text{Ar}^+$  and  $\text{Kr}^+$ , respectively. These energies were chosen so that the momenta of the three ions were identical ( $16.7 (\text{amu keV})^{1/2}$ ). From figures 4–6 it is evident that the trends in the degree of NSRED are consistent with those of the vacancy production rates. This consistency of trends indicates that the derived trends of excess vacancy clusters, or  $\bar{\Sigma}$ , induced by ion pre-irradiation are correct. Nevertheless, a discrepancy exists between the  $\bar{\Sigma}$ –mass curves and the  $V$ –mass curves. This can be attributed to the following.

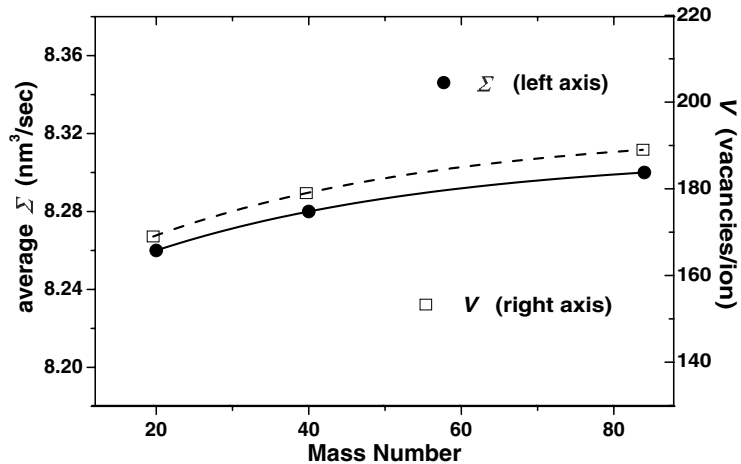


**Figure 4.** Average  $\Sigma$  and vacancy production rate  $V$  versus mass number. The ion energies of  $\text{Ne}^+$ ,  $\text{Ar}^+$  and  $\text{Kr}^+$  are 7 keV. The curves were drawn to guide the eye.

- (1) TRIM uses amorphous targets while crystalline  $\text{MgO}(100)$  substrates were used in this work.
- (2) Vacancies in the form of vacancy clusters are responsible for NSRED and the contributions from mono-vacancies are negligible, while  $V$  includes all of the vacancies produced.

Examination of figure 6 reveals that, when  $\bar{\Sigma}$  is close to 0, the corresponding vacancy production rate is still appreciable (50 vacancies/ion). This indicates that there exists a threshold value of vacancy production rate below which vacancy clusters cannot be formed and NSRED does not appear. This is understandable for vacancy clustering since a critical number of vacancies is necessary, otherwise the density of vacancies is so dilute that the chance of vacancies joining together, or clustering, is negligibly small. Similar phenomena have been observed for the formation of vacancy clusters in Si by  $\text{He}^+$  implantation (Brusa *et al* 2000). We can conclude that the vacancy clusters induced by ion pre-irradiation play a key role in promoting NSRED. The mono-vacancies formed by thermal dissociation of vacancy clusters are responsible for the enhanced cation diffusion observed (figure 2).

### 3.3. Post-irradiation annealing effect on NSRED

Since vacancy clusters are responsible for NSRED as emphasized above, from TED results (Moller *et al* 1998), a similar prediction is that annealing the ion pre-irradiated  $\text{MgO}$ , i.e. post-irradiation annealing, causes a reduction of the vacancy clusters both in number and size, leading to the reduction of subsequent NSRED with increasing post-annealing temperature and time. Figure 7 shows the Ti depth profiles for irradiated samples followed by annealing at a temperature of  $T_{\text{pa}} = 1000^\circ\text{C}$  at various post-annealing times ( $\tau = 5, 10$  and 20 min), together with their fitting curves. Data fitting was carried out by using the model in section 3.1 and  $\bar{\Sigma}$  for evaluating the degree of NSRED. The sample identification is  $\text{Ti}/\text{Ar}/\text{MgO}(T, \tau)$ , where  $\text{MgO}$  has been pre-irradiated with 7 keV  $\text{Ar}^+$  for a dose of  $5 \times 10^{15} \text{ cm}^{-2}$ , followed by post-irradiation annealing at a temperature ( $T_{\text{pa}}$ ) for  $\tau$  min before evaporation and diffusion. Diffusion was conducted at  $1000^\circ\text{C}$  for 6 min. In order to show the results more clearly, the data for  $\tau = 5$  min are not included in this figure. As expected, with increasing  $\tau$ , the degree of NSRED decreases. The corresponding quantitative results are shown in table 2. Similar

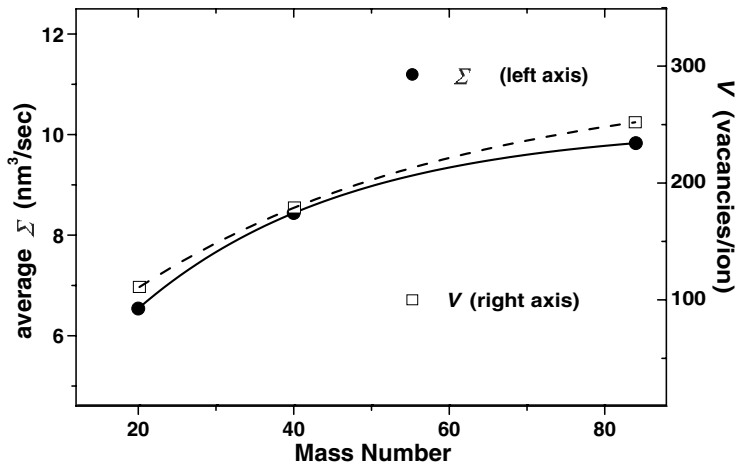


**Figure 5.** Average  $\Sigma$  and vacancy production rate  $V$  versus mass number. The ion energies selected for  $\text{Ne}^+$ ,  $\text{Ar}^+$  and  $\text{Kr}^+$  give identical ion penetration ranges (7.1 nm). The curves were drawn to guide the eye.

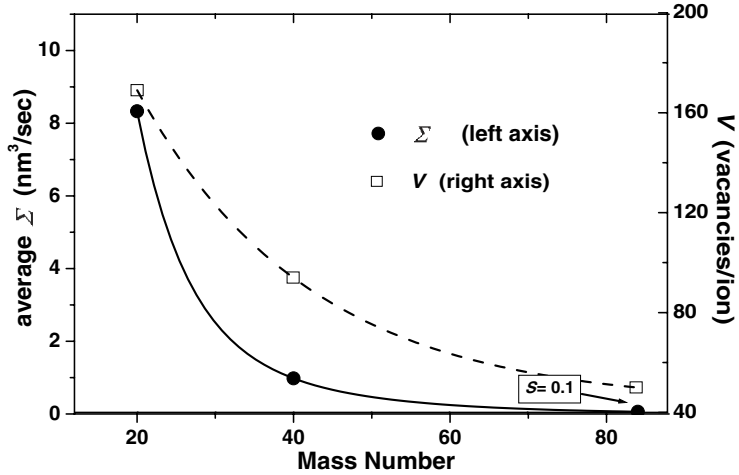


**Figure 6.** Average  $\Sigma$  and vacancy production rate  $V$  versus mass number. The ion energies selected for  $\text{Ne}^+$ ,  $\text{Ar}^+$  and  $\text{Kr}^+$  give identical momenta ( $16.7 \text{ (amu keV)}^{1/2}$ ). The curves were drawn to guide the eye.

trends were obtained for  $T_{\text{pa}} = 800$  and  $900^\circ\text{C}$  (table 2). Furthermore, for the same  $\tau$ , from  $T_{\text{pa}}$  of 800 to  $1000^\circ\text{C}$ , the value of  $\bar{\Sigma}$  decreases with increasing  $T_{\text{pa}}$ . This result also conforms to the expectation transferred from TED results (Moller *et al* 1998). However, at higher  $T_{\text{pa}}$ , such as  $1100^\circ\text{C}$ , post-annealing generates an unexpected result, as shown in figure 8. It is observed that, for  $\text{Ti}/\text{Ar}/\text{MgO}(1100^\circ\text{C}, 10)$ , the diffusion was even more enhanced than that without post-annealing ( $\text{Ti}/\text{Ar}/\text{MgO}$ ). When the post-annealing time was prolonged to 20 min, i.e.  $\text{Ti}/\text{Ar}/\text{MgO}(1100^\circ\text{C}, 20)$ , this diffusion enhancement was reduced, but is still slightly greater than that of  $\text{Ti}/\text{Ar}/\text{MgO}$ . Quantitative analysis of this data are listed in table 2. For all the data, the fitting parameters are  $L = 14.9 \pm 0.2 \text{ nm}$  and  $\lambda^2 = 22.0 \pm 0.0 \text{ nm}^2$ . The data for  $\text{Ti}/\text{MgO}(1100^\circ\text{C}, 20)$  in figure 8 nearly coincide with that of  $\text{Ti}/\text{MgO}$ . This means

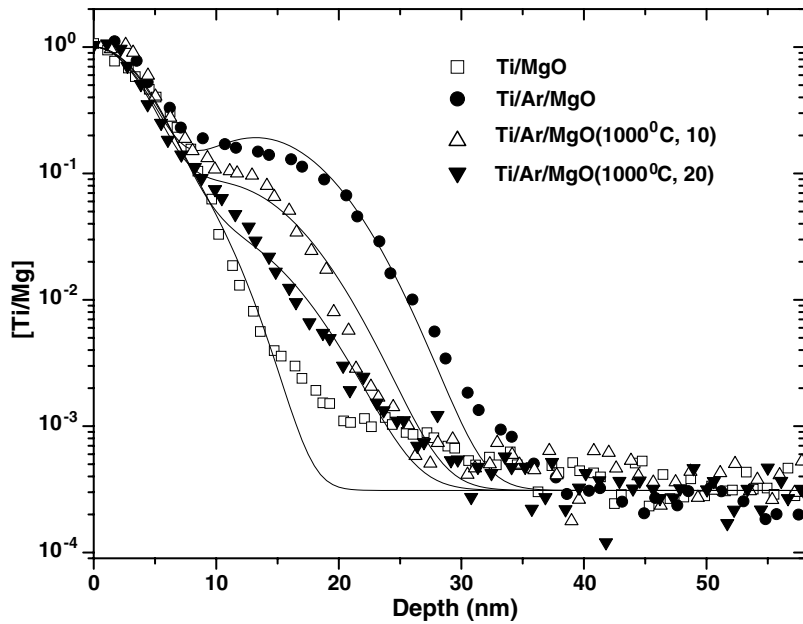


**Figure 7.** SIMS depth profiles of [Ti/Mg] for diffusion samples post-annealed at 1000 °C together with the data for the sample without pre-irradiation (Ti/MgO) and that without post-irradiation annealing (Ti/Ar/MgO).

**Table 2.** NSRED values as a function of post-annealing temperature and time.  $\bar{\Sigma}$ s are in  $\text{nm}^3 \text{ s}^{-1}$ .

Post-annealing temperature ( $T_{\text{pa}}$ )	800 °C	900 °C	1000 °C	1100 °C
$\bar{\Sigma}$ ( $\tau = 0 \text{ min}$ )	7.5	7.5	7.5	7.5
$\bar{\Sigma}$ ( $\tau = 5 \text{ min}$ )	6.4	—	5.1	—
$\bar{\Sigma}$ ( $\tau = 10 \text{ min}$ )	5.7	5.0	3.6	29.6
$\bar{\Sigma}$ ( $\tau = 20 \text{ min}$ )	4.1	3.1	2.1	9.2

that additional annealing of MgO at 1100 °C for 20 min in UHV did not change the distribution of defects for Ti diffusion: hence the unusual increase of  $\Sigma$  for Ti/Ar/MgO(1100 °C, 10) and Ti/Ar/MgO(1100 °C, 20) is directly related to the deformation caused by ion pre-irradiation.

For  $T_{\text{pa}} = 800, 900$  and  $1000$  °C, the value of  $\bar{\Sigma}$  versus  $\tau$  roughly followed an exponential decay form similar to equation (3). However, the unusual enhanced diffusion at  $T_{\text{pa}} = 1100$  °C indicated that vacancy cluster evolution with post-annealing time was not the same as that for Si{311} interstitial clusters in Si, where an exponential decay of {311} clusters with annealing time was observed (Moller *et al* 1998). We now estimate the size of vacancy clusters that contribute predominantly to NSRED. Van Sambeek *et al* (1998) found that the thermal dissociation of Mg vacancy clusters promotes RED and that the dissociation energy is 4.1 eV. From previous calculations (Mackrodt and Stewart 1977, Zinkle and Kinoshita 1997, Busker *et al* 2000), it was shown that the dissociation of one Mg divacancy in MgO requires 3.9–4.4 eV. Therefore, the vacancy clusters for Ti NSRED in MgO are likely to be mainly Mg divacancies.

Vacancy clusters larger than divacancies in size also exist after ion pre-irradiation (Kapinos and Platonov 1985a, 1985b, 1987, Pramanik and Seidman 1983, Diaz de la Rubia *et al*

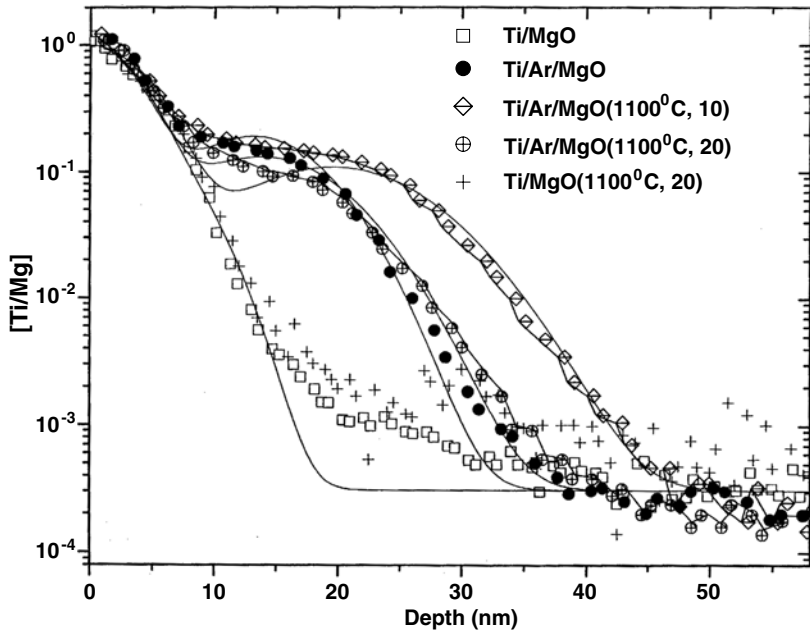


**Figure 8.** SIMS depth profiles of [Ti/Mg] for diffusion samples post-annealed at 1100 °C together with the data for the sample without pre-irradiation (Ti/MgO) and that without post-irradiation annealing (Ti/Ar/MgO). The sample for which the MgO substrate has been annealed at 1100 °C for 20 min in UHV (Ti/MgO(1100 °C, 20)) shows a similar diffusion behaviour to that of Ti/MgO.

1990). For convenience, we refer to these extended vacancies as larger vacancy clusters, or LVCs. During post-annealing, these LVCs also experience thermal dissociation, which tends to increase the number of divacancies. Therefore, to describe the post-annealing effect in NSRED, in addition to the divacancy annihilation process, a divacancy creation mechanism should also be considered. The change in the number of divacancies with post-annealing time  $\tau$  can be written as

$$\frac{\partial \Pi}{\partial \tau} = -k\Pi + f\left(-\frac{\partial \Omega}{\partial \tau}\right) + g\left(-\frac{\partial \Pi}{\partial \tau}\right), \quad (5)$$

where  $\Pi$  reflects the number of divacancies, which is proportional to  $\Sigma$ ,  $k$  is the dissociation rate,  $-\partial \Omega / \partial \tau$  is the dissociation rate of LVCs with  $\Omega$  being the number of LVCs and  $f$  represents the fraction of dissociated LVCs that contribute to divacancy creation. The third term on the right side of equation (5) denotes the re-clustering of divacancies during divacancy dissociation,  $g < 1$ . Since various size LVCs can exist, the second term on the right side of equation (5) should be replaced with  $\sum_{n>2} f_n (-\partial \Omega / \partial \tau)_n$ , where  $n$  denotes the LVC size. However, the distribution of vacancy clusters is unknown. Since we are only pursuing a qualitative analysis, we assume that effectively only one size of LVC exists, therefore the following discussions are based only on equation (5). This will not change the general conclusions that have been made. Equation (5) can be rewritten as

$$\frac{\partial \Pi}{\partial \tau} = -\frac{k}{1+g}\Sigma + \frac{f}{1+g}\left(-\frac{\partial \Omega}{\partial \tau}\right). \quad (6)$$

Similarly for the effective LVC, we have

$$\frac{\partial \Omega}{\partial \tau} = -\frac{\eta}{1+\alpha} \Omega + \frac{\beta}{1+\alpha} \left( -\frac{\partial \Pi}{\partial \tau} \right), \quad (7)$$

where  $\eta$  is the thermal dissociation rate constant of LVCs, which also represents the rate constant for divacancy creation. The second term reflects the contribution from the dissociation of divacancies to the increase in LVCs,  $\beta$  represents the fraction of dissociated divacancies that contribute to the increase in LVCs and  $\alpha$  ( $< 1$ ) is the re-clustering fraction of the effective LVCs. Therefore, in order to know how  $\Pi$  evolves during post-annealing, the coupled equations (6) and (7) should be solved. The values of  $k$  and  $\eta$  are  $T_{\text{pa}}$ -dependent and follow an Arrhenius expression. Since  $\eta$  represents the dissociation of LVCs which have larger dissociation energies than those for divacancies (Mackrodt and Stewart 1977, Zinkle and Kinoshita 1997), it can be inferred that  $\eta/k$  also obeys an Arrhenius expression as

$$\eta/k = A \exp(-\Delta E_d/k_B T_{\text{pa}}), \quad (8)$$

where  $A$  is a constant,  $\Delta E_d$  ( $> 0$ ) is the difference in the dissociation energies of LVCs and divacancies and  $k_B$  is the Boltzmann constant. The contribution of the ratio  $f/\beta$  is not arbitrary. In order to dissociate a  $n$ -size LVCs and form divacancies, the maximum value of  $f$  is  $n/2$  if mono-vacancies are not lost. Similarly,  $\beta$  is  $2/n$ . During the dissociation of vacancy clusters, the loss of mono-vacancies is inevitable as they move relatively fast and can be annihilated at various sinks such as grain boundaries and surfaces, hence,  $f$  and  $\beta$  cannot reach their maximum values. However, their ratio  $f/\beta$  can still be taken as  $\sim (n/2)^2$ . For instance, if the size of the effective LVC is 3, then  $f/\beta$  is  $\sim (3/2)^2 = 2.25$ ; if  $n = 4$ ,  $f/\beta \sim 4.0$ .

The post-annealing results can be explained by using equations (6)–(8). For qualitative analysis, three post-annealing temperatures were considered in the order of  $T_{\text{pa}0} > T_{\text{pa}1} > T_{\text{pa}2}$ . The initial number of divacancies and LVCs induced by ion pre-irradiations are assumed to be  $\Pi_0 = 100$  and  $\Omega_0 = 400$ , respectively. The values of  $k$  for  $T_{\text{pa}} = T_{\text{pa}0}$ ,  $T_{\text{pa}1}$  and  $T_{\text{pa}2}$  are 0.55, 0.25 and 0.15, respectively, and those of  $\eta$  are 0.5, 0.05 and 0.01, respectively, all in arbitrary units. Other quantities are:  $g = 0$ ,  $\alpha = 0.1$ ,  $f = 0.45$  and  $\beta = 0.11$ , i.e. the size of the effective LVCs is assumed to be 4, which is not unrealistic. It was found later that the size of effective LVCs, or the value of the ratio  $f/\beta$ , and the choices of  $g$  and  $\alpha$  are not critical in the interpretation of the experimental results. The selections of the values for  $\Pi_0$  and  $\Omega_0$  can be somewhat arbitrary, but those of  $k$  and  $\eta$  should obey the relationship described by equation (8) and the ratio of dissociation energies derived from  $\eta$ 's and  $k$ 's should be within a reasonable range. Since  $\eta$  and  $k$  follow Arrhenius expressions, plotting  $\ln \eta$  and  $\ln k$  versus  $1/T_{\text{pa}}$  yield dissociation energies for effective LVCs and divacancies: hence their ratio is obtained. For the parameters of  $T_{\text{pa}}$ ,  $\eta$  and  $k$  chosen above, this ratio is 1.4, which is rational in terms of theoretical models (Busker *et al* 2000). Equation (8) is the key factor in explaining the observed unusual diffusion enhancement at high  $T_{\text{pa}}$ . In figure 9, the curves 1, 2 and 3 are for  $k = 0.55$ , 0.25 and 0.15 with  $\eta = 0$  at  $T_{\text{pa}} = T_{\text{pa}0}$ ,  $T_{\text{pa}1}$  and  $T_{\text{pa}2}$ , respectively. These curves behave in accordance with our intuitive rationalization of the post-annealing effect, that is, the higher the annealing temperature and the longer the annealing time, the more the defects are annealed out. This is in accord with TED results (Moller *et al* 1998) and the annealing effect on cation diffusion in  $\text{Al}_2\text{O}_3$  (Moya *et al* 1998). However, when the divacancy creation mechanism begins, i.e.  $\eta \neq 0$ , this trend changes. Curves 4, 5 and 6 are for  $k = 0.55$ , 0.25 and 0.15 with  $\eta = 0.5$ , 0.05 and 0.01, respectively. It is observed that curves 5 and 6 for  $T_{\text{pa}} = T_{\text{pa}1}$  and  $T_{\text{pa}2}$  are close together as compared to those of 2 and 3. For  $T_{\text{pa}} = T_{\text{pa}0}$  (curve 4), the  $\eta$  increases so rapidly that, in the early stage of post-annealing, the number of divacancies increases with  $\tau$ , reaches a maximum at  $\tau \sim 0.98$  and then drops down more quickly than the curves of  $T_{\text{pa}} = T_{\text{pa}1}$  and  $T_{\text{pa}2}$  (curves 5 and 6), crossing them at  $\tau \sim 4.0$  and 3.8, respectively.

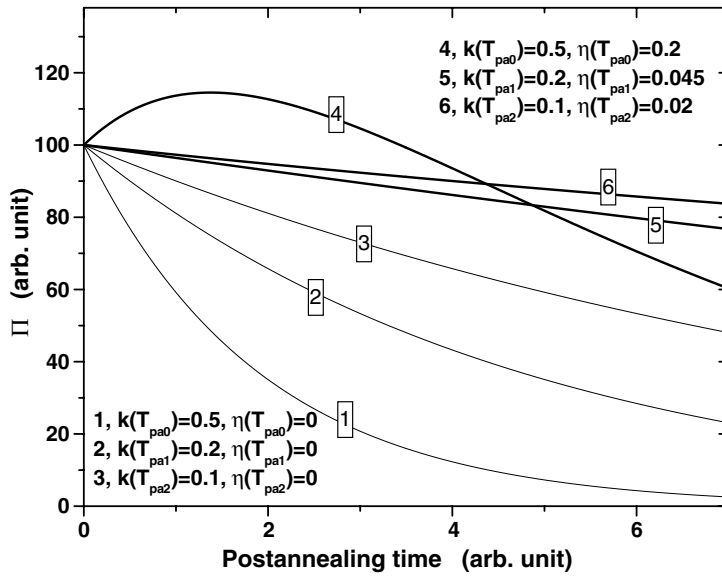


**Figure 9.** Curves 1, 2 and 3 represent the  $\Pi$  (divacancy number) evolution with post-irradiation annealing time at  $T_{\text{pa}} = T_{\text{pa}0}$ ,  $T_{\text{pa}1}$  and  $T_{\text{pa}2}$  ( $T_{\text{pa}0} > T_{\text{pa}1} > T_{\text{pa}2}$ ), respectively, without considering the divacancy creation mechanism. Their behaviours conform to the intuitive understanding of the post-annealing effect. When divacancy creation sets in, the corresponding trends of  $\Pi$  change as illustrated by curves 4, 5 and 6. The evolution of curve 4 explains the unusual diffusion enhancement observed in figure 8.

These results illustrate that  $\eta$  increases more rapidly than  $k$  with increasing  $T_{\text{pa}}$  (equation (8)). At higher  $T_{\text{pa}}$ , such as 1100 °C, the net number of divacancies is larger in the early stage of post-annealing, leading to an unusual enhancement of the subsequent diffusion as compared to the sample without post-annealing. This is the case of Ti/Ar/MgO(1100 °C, 10). Beyond this maximum level, further post-annealing reduces the number of divacancies and implicit diffusion, as observed for Ti/Ar/MgO(1100 °C, 20).

Divacancies are now regarded as the main defects that are responsible for promoting NSRED. In principle, dissociation of LVCs such as tri- and tetra-vacancies are equally capable of enhancing the diffusion. We have tested this point by comparing the mono-vacancy production rate due to thermal dissociation of divacancies with that due to trivacancies at the diffusion temperature of 1000 °C (Lu *et al* 2002c). It was found that the probability of obtaining the same amount of mono-vacancies from trivacancies is only  $3.5 \times 10^{-12}$  times that from divacancies. Hence the contributions from larger vacancy clusters can be completely ignored. Therefore, it is proper to focus on divacancy densities and disregard the direct contributions from LVCs.

In summary, our interpretation assumes that, in addition to the annihilation process of divacancies for NSRED, there exists a divacancy creation mechanism due to the thermal dissociation of LVCs during post-irradiation annealing. This analysis is of qualitative importance. It is not sufficient for a precise description of the post-annealing effect. However, the analysis is basically correct as it is derived from the experimental facts and basic physical considerations, i.e. in addition to the annihilation process of divacancies for NSRED, there exists a divacancy creation mechanism due to thermal dissociation of LVCs during post-irradiation annealing.

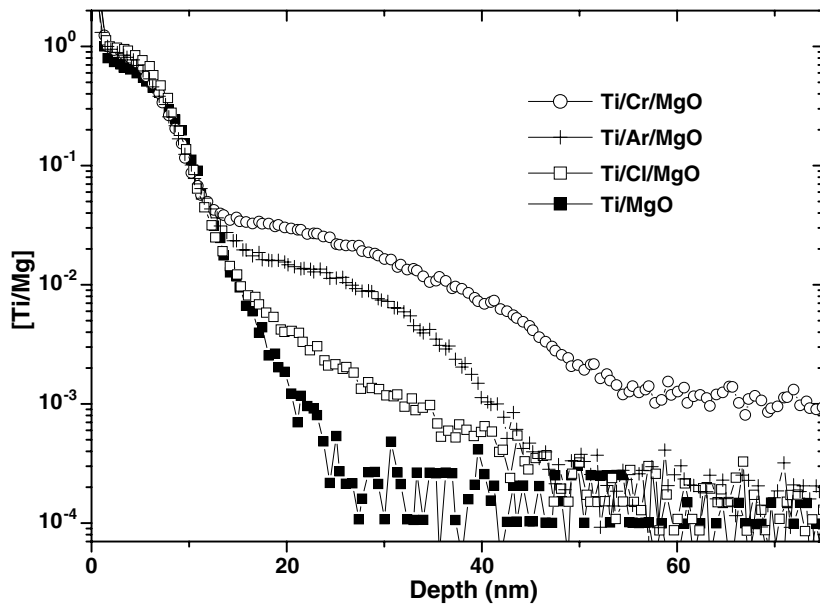


**Figure 10.** SIMS depth profiles of the intensity ratio  $[\text{Ti}/\text{Mg}]$  for the  $\text{Ti}/\text{MgO}$ ,  $\text{Ti}/\text{Ar}/\text{MgO}$ ,  $\text{Ti}/\text{Cl}/\text{MgO}$  and  $\text{Ti}/\text{Cr}/\text{MgO}$  samples after diffusion at  $1000^\circ\text{C}$  for 6 min.

### 3.4. Chemical effect of NSRED

This section deals with another unique feature of NSRED, i.e. the chemical effect. Ti diffusion profiles in  $\text{MgO}(100)$  pre-irradiated with 7 keV  $^{40}\text{Ar}^+$ ,  $^{35}\text{Cl}^+$  and  $^{52}\text{Cr}^+$  are presented in figure 10 and labelled as  $\text{Ti}/\text{Ar}/\text{MgO}$ ,  $\text{Ti}/\text{Cl}/\text{MgO}$  and  $\text{Ti}/\text{Cr}/\text{MgO}$ , respectively. For all of the samples, the ion dose was  $5 \times 10^{15}$  ions  $\text{cm}^{-2}$  and the diffusion was conducted at  $1000^\circ\text{C}$  for 6 min. The irradiating ions were chosen because their masses and their ballistic behaviours are similar, as shown by the TRIM simulation in figure 11. However, their chemical properties are very different. The stable chemical state for Cl is  $\text{Cl}^-$ , while that for Cr is  $\text{Cr}^{3+}$ , and Ar is chemically inert. Initially, it has been assumed that enhanced diffusion is related only to the ballistic properties of the irradiating ions and their chemical properties are unimportant for conventional RED. The chemical properties have been ignored. The existing theories have also treated this situation (Diens and Damask 1958, Sizmann 1978, Van Sambeek *et al* 1998). However, for NSRED, the enhanced diffusion evidently depends on the chemical properties of the ions as shown in figure 10. The degree of NSRED follows the order of  $\text{Ti}/\text{Cr}/\text{MgO} > \text{Ti}/\text{Ar}/\text{MgO} > \text{Ti}/\text{Cl}/\text{MgO}$ . The irradiating ions can attain their most stable valence state within the  $\text{MgO}$  lattice through electron transfer processes (Mrowec 1980). In order to maintain electrical neutrality of the  $\text{MgO}$  (100) crystal, the presence of the  $\text{Cr}^{3+}$  impurity in  $\text{MgO}$  creates excess Mg vacancies (Yang and Flynn 1994). Through a similar analysis, the same was also found for  $\text{Cl}^-$  and  $\text{Ar}^0$  present as impurities in  $\text{MgO}$  (Lu *et al* 2001). Since the residual concentration order in  $\text{MgO}$  is  $\text{Ar} < \text{Cl} < \text{Cr}$  due to the outdiffusion of Ar and Cl, which was verified by SIMS depth profile data (Lu *et al* 2003), the electrical neutrality requirement leads to the ordering  $\text{Ti}/\text{Cr}/\text{MgO} > \text{Ti}/\text{Cl}/\text{MgO} > \text{Ti}/\text{Ar}/\text{MgO}$  for the degree of NSRED. This is contradictory to the experimental results. Other effects, such as lattice deformation and chemical reactions, cannot explain the observed order for the degree of NSRED either (Lu *et al* 2001).

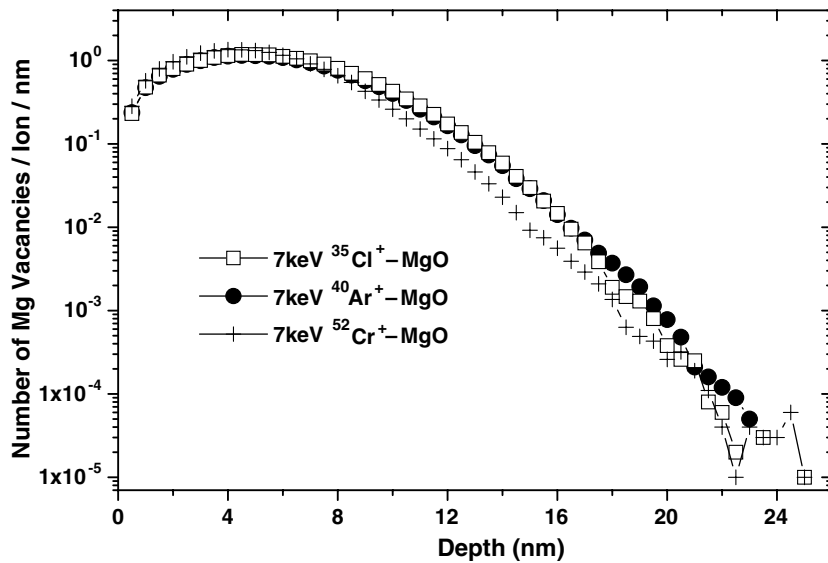


**Figure 11.** Depth distributions of Mg vacancies induced by irradiations of 7 keV  $\text{Ar}^+$ ,  $\text{Cl}^+$  and  $\text{Cr}^+$  in  $\text{MgO}$ , as obtained by TRIM simulations.

The post-irradiation annealing effect in NSRED aforementioned reveals that the size distribution of Mg vacancy clusters affects the subsequent diffusion behaviour. This result provides a clue for the interpretation of the chemical effect in NSRED. The defect structures induced by  $\text{Ar}^+$ -,  $\text{Cl}^+$ - and  $\text{Cr}^+$ -irradiated  $\text{MgO}$  may be different in spite of their similar ballistic behaviours. In a series of papers on the nucleation of vacancy clusters in the cascade range, Kapinos and Platonov (1985a, 1985b, 1987) found that immediately after the collision stage of ion irradiation ( $10^{-15}$ – $10^{-13}$  s), the centre of the collision cascade, or implantation profile, is enriched in vacancies and the nascent interstitials are located on the periphery. This result has also been confirmed by more recent molecular dynamic studies (Nordlund and Averback 1997). The thermal spike formed in the centre of the cascade due to ion irradiation leads to this defect structure. The following thermal relaxation stage of the energetic cascade requires  $>10^{-11}$  s, during which time vacancy clusters are formed in the central region of the cascade zone. It is noted that, before thermal relaxation, the defect structure formed is determined by the ballistic behaviour of the irradiating ion and is not related to chemical reactions. Therefore, immediately after collision, the distributions of Mg vacancies and interstitials induced by  $\text{Ar}^+$ ,  $\text{Cl}^+$  and  $\text{Cr}^+$  irradiations should be nearly the same due to their similar masses, as illustrated in figures 12(a)–(c) for the ‘before relaxation’ stage. During the thermal relaxation process, some of the Mg interstitials and vacancies tend to annihilate each other by recombination through migration. The implanted Cl is likely to react with the interstitial Mg to form  $\text{MgCl}_x$  and/or  $\text{MgO}_y\text{Cl}_z$  compounds (Weast 1995), preventing Mg interstitials from migrating towards Mg vacancies for recombination. Therefore more Mg vacancies survive the recombination after thermal relaxation. Consequently, the  $\text{Cl}^+$ -irradiated  $\text{MgO}$  tends to have larger Mg vacancy clusters than  $\text{Ar}^+$ -irradiated  $\text{MgO}$ . This is shown in figures 12(a) and (b) for the ‘after relaxation’ stage. On the other hand, for the implanted  $\text{Cr}^+$ , instead of capturing Mg interstitials and hence preventing them from annihilating Mg vacancies, Cr itself tends to take the Mg vacancy position due to its similar ion size (the diameters are  $\text{Cr}^{3+} = 0.123$  nm and  $\text{Mg}^{2+} = 0.144$  nm) and electrical polarity to Mg (Lof 1987). Therefore,

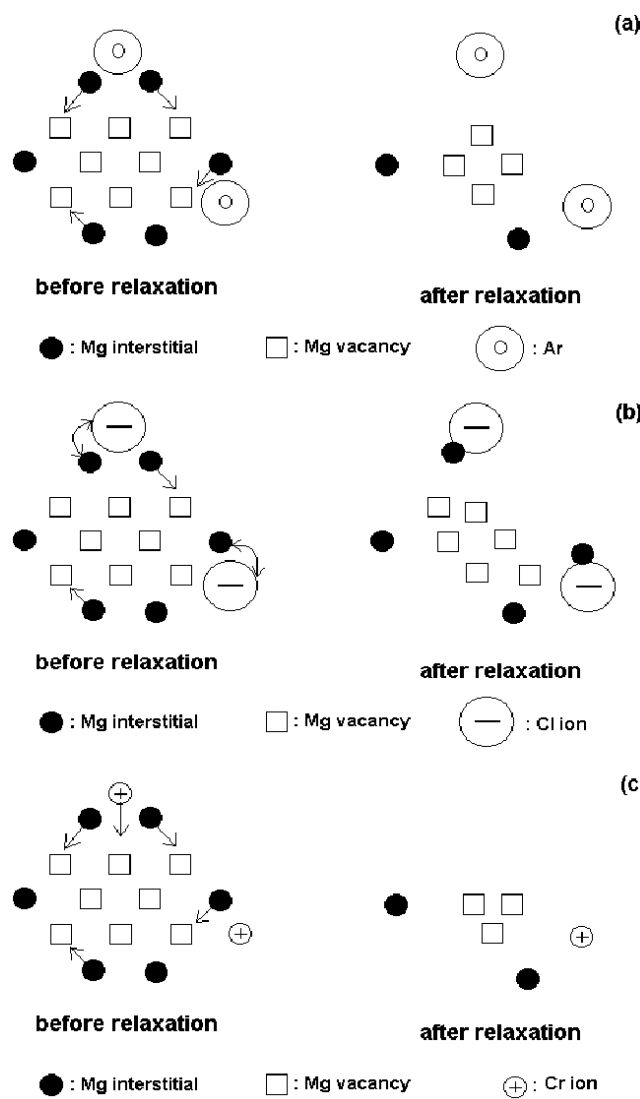


**Figure 12.** Schematic illustration of the effect of the chemical properties of the pre-irradiating ion on the formation of Mg vacancy clusters in MgO. Statistically, the size of Mg vacancy clusters formed in MgO pre-irradiated with  $\text{Ar}^+$ ,  $\text{Cl}^+$  and  $\text{Cr}^+$  follows the trend  $\text{Cl}^+ > \text{Ar}^+ > \text{Cr}^+$  after thermal relaxation, in spite of their very close ballistic behaviours.

as compared to Ar, more Mg vacancies are annihilated after thermal relaxation and the  $\text{Cr}^+$ -irradiated MgO tends to have smaller Mg vacancy clusters than the  $\text{Ar}^+$ -irradiated MgO as illustrated in figures 12(a) and (c) for the 'after relaxation' stage. It is known that mono-vacancies released by thermal dissociation of Mg vacancy clusters promote NSRED. Since the small Mg vacancy clusters have lower dissociation energies (Busker *et al* 2000), they release mono-vacancies more efficiently upon annealing, as mentioned in section 3.3. Hence diffusion is more enhanced for a short time diffusion. That is what we observed in figure 10 as  $\text{Ti/Cr/MgO} > \text{Ti/Ar/MgO} > \text{Ti/Cl/MgO}$  for the degree of NSRED. However, after a

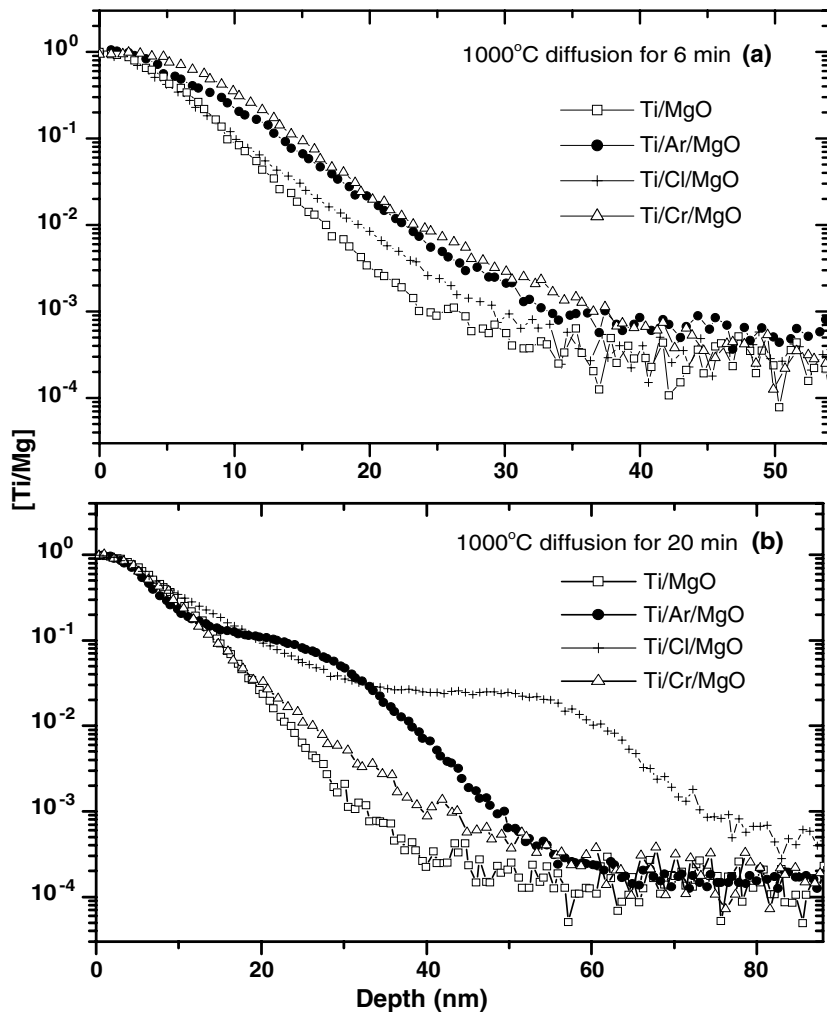


**Figure 13.** (a) SIMS depth profiles of the intensity ratio  $[Ti/Mg]$  for Ti diffusion at  $1000\text{ }^{\circ}\text{C}$  for 6 min in  $\text{MgO}$  and  $\text{MgO}$  pre-irradiated with 7 keV  $\text{Ar}^+$ ,  $\text{Cl}^+$  and  $\text{Cr}^+$ . (b) Corresponding results for 20 min.

prolonged diffusion time when most vacancy clusters are dissociated and the stored vacancies are released, it is predictable from the schematic of figure 12 that the order of the NSRED degree should be reversed as  $\text{Ti/Cl/MgO} > \text{Ti/Ar/MgO} > \text{Ti/Cr/MgO}$ . This point was tested by measuring diffusion profiles for samples after diffusion at  $1000\text{ }^{\circ}\text{C}$  for 6 and 20 min as shown in figure 13. It is seen that the NSRED trend exactly agrees with the prediction, i.e.  $\text{Ti/Cl/MgO} > \text{Ti/Ar/MgO} > \text{Ti/Cr/MgO}$  for 20 min annealing. This behaviour supports our modified vacancy clustering model for chemical effects.

Transmission electron microscopy (TEM) has been applied to obtain direct evidence for the proposed model. Unfortunately, the TEM was not able to distinguish between Mg and O vacancy clusters. Partyka *et al* (2001) developed the technique of grazing incidence diffuse x-ray scattering to investigate defect structures in silicon which, combined with computer simulations, may be applicable to test the modified vacancy clustering model. Recently, by

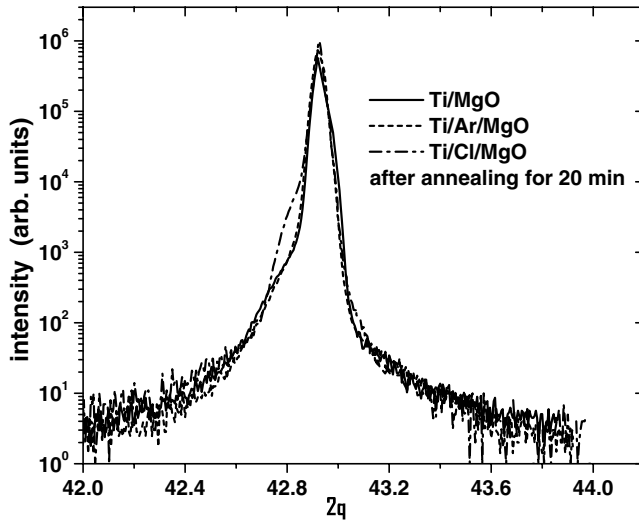


**Figure 14.** High resolution x-ray diffraction spectra for Ti/MgO, Ti/Ar/MgO and Ti/Cl/MgO after diffusion at 1000 °C for 20 min. The residual strain due to ion pre-irradiation for Ti/Cl/MgO is larger than that for Ti/Ar/MgO, indicating that the vacancy clusters in MgO induced by Cl<sup>+</sup> ion irradiation are larger in size than those induced by Ar<sup>+</sup>.

using high resolution x-ray diffraction (HRXRD), Lupu (2003) found that, after diffusion annealing of Ti/MgO, Ti/Ar/MgO and Ti/Cl/MgO at 1000 °C for 20 min, the residual strain by ion irradiation for Ti/Cl/MgO was still large, while for Ti/Ar/MgO it was close to that of Ti/MgO. This is shown in figure 14. The main peak at  $2\theta \sim 42.9^\circ$  corresponds to the (200) reflection characteristic of the pure MgO (100) surface. The shoulder structure observed at slightly lower  $2\theta$  values (42.5(Ar) and 42.7(Cl)) provides information regarding the extent of the lattice deformation in the modified MgO samples. This result indicates that, after annealing Ti/Ar/MgO for 20 min, the ion-irradiation-induced defects are nearly annealed out; only those induced by Ti doping remain. However, for Ti/Cl/MgO, the ion-irradiated-induced defects still exist after annealing. This is consistent with the physical model of figure 12, i.e. statistically the vacancy clusters induced by Cl<sup>+</sup> irradiation are larger in size than those induced by Ar<sup>+</sup> irradiation. Hence, it is expected that more Ti/Cl/MgO vacancy clusters survive the thermal annealing.

### 3.5. Sensitivity of NSRED to defects and impurities

Since diffusion is extremely sensitive to intrinsic defects and impurities in the substrate (Sangster and Stoneham 1994, Yang and Flynn 1994, Moya *et al* 1998), comparisons of diffusion data derived from substrates obtained from different sources can be misleading. This was found to be the case for MgO. Furthermore, it was found that Ti diffusion behaviour in one wafer of MgO may be slightly different in another wafer, even if the wafers were obtained from the same manufacturer. This is because the residual impurity distributions vary from one wafer to another, as shown by our SIMS data (Lu *et al* 2002d). In view of this, the MgO samples used for each of our systematic series of experiments were cut from a single 50 × 50 × 0.5 mm<sup>2</sup> MgO wafer. For example, a single wafer was used for the results of sections 3.1 and 3.2, while a different wafer was used for the results of section 3.3. The different diffusion behaviours of Ti in different MgO wafers are reflected by

differences in their NSRED parameters, i.e.  $D_1$ ,  $L$ ,  $\lambda^2$ ,  $\Sigma$  and  $\bar{\Sigma}$ . An example is the value of  $\bar{\Sigma}$  in tables 1 ( $\bar{\Sigma} = 8.3 \text{ nm}^3 \text{ s}^{-1}$ ) and 2 ( $\bar{\Sigma} = 7.5 \text{ nm}^3 \text{ s}^{-1}$ ) for the Ti/Ar/MgO sample. Therefore, quantitative data comparison between sections 3.1 and 3.2 is reasonable and also within section 3.3, but comparison of data from sections 3.1 and 3.2 with 3.3 will contain systematic errors. In section 3.4, the MgO used in figures 10 and 13(a) and (b) was from different wafers. Hence the small differences in the observed detailed diffusion behaviours exist for 6 min annealing time (Lu *et al* 2002d), although the NSRED order remains the same. For the chemical effect described in section 3.4, quantification of the degree of NSRED was not possible due to limitations in our data analysis software. Improvements are currently underway to correct this deficiency.

The fitting curves of the diffusion profiles in the low concentration region for Ti/MgO in figures 1 and 7 exhibit considerable deviation from the experimental data. This is because, in the model of section 3.1, only the main diffusion process, i.e. bulk diffusion, is included and the less significant dislocation diffusion is not considered. Dislocation diffusion contributes appreciably only to the low concentration profile (Weiss *et al* 2000, Lu *et al* 2001), which is of minor importance for future applications.

#### 4. Conclusions and outlook

This review is focused on our work on a new type of radiation-enhanced diffusion, i.e. non-steady-state radiation-enhanced diffusion, or NSRED. NSRED differs from conventional RED in the diffusion–irradiation procedure, distribution of excess defects and sample geometry. These differences make the existing RED theories unsuitable for describing NSRED. A phenomenological model was developed in sections 3.1 and 3.2 to quantify NSRED based on a concept of depth-dependent diffusion coefficients. It was found that vacancy clusters play a key role in NSRED instead of mono-vacancies, as in conventional RED. This property leads to two effects that are unique to NSRED, i.e. the post-irradiation annealing effect (section 3.3) and the chemical effect (section 3.4). The post-annealing effect shows that post-irradiation annealing of the substrate not only reduces the subsequent diffusion as normally expected but, under some circumstances, it enhances the diffusion as well. The chemical effect reveals another important fact, i.e. the chemical properties of irradiating ions can significantly affect the subsequent diffusion. This has not been observed in conventional RED. The physics underlying these two effects is that, for NSRED, vacancy clusters instead of mono-vacancies are responsible for diffusion.

The adopted diffusion–irradiation procedure and the sample geometry of NSRED afford great flexibility for this new diffusion technique in future applications. The parameters and approaches available for NSRED provide excellent control of the diffusion behaviour in the substrate. For example, the depth profile shape, density and diffusion range of diffusants can be manipulated by adjusting the location and density distribution of vacancy clusters by varying the ion energy, mass, chemical properties, dose and irradiation procedure. The irradiation procedure consists of the use of selected irradiation conditions to achieve the desired implant distributions. For example, irradiation with ion beams from higher energy to lower energy, in order to create a nearly uniform distribution of vacancy clusters or other desired distributions of vacancy clusters from the near-surface region to a preset depth. The flexibility in its diffusion–irradiation procedure, sample geometry and versatility in manipulating diffusion render NSRED a promising technique for future applications such as improvements of optical and mechanical properties of oxides through well-controlled metallic ion doping, where the doping distributions and densities are of critical importance (e.g. McHargue 1998).

### Acknowledgments

This material is based on work supported by the R A Welch Foundation under grant no E656 and the Texas Advanced Research Program under proposal no 003652-0002-2001. We thank M Weiss, S M Lee, V J Styve, Y Meng and S S Perry for assistance in this work.

### References

Albayati A H, Marton D, Todorov S S, Boyd K J, Rabalais J W, Armour D G, Gordon J S and Duller G 1994 *Rev. Sci. Instrum.* **65** 2680

Bedrossian P J, Caturla M J and Diaz de la Rubia T 1997 *Appl. Phys. Lett.* **70** 176

Bigarre J, Fayeulle S and Treheux D 1997 *J. Appl. Phys.* **82** 3740

Borg R J and Diens G J 1988 *An Introduction to Solid State Diffusion* (San Diego, CA: Academic)

Brusa R S, Karwasz G P, Tieno N, Zecca A, Corni F, Tonini R and Ottaviani G 2000 *Phys. Rev. B* **61** 10154

Busker G, van Huis M A, Grimes R W and van Veen A 2000 *Nucl. Instrum. Methods B* **171** 528

Canut B, Dupin J P, Gea L, Ramos S M and Thevenard P 1991 *Nucl. Instrum. Methods B* **59/60** 1211

Cowen N E, Janssen K T F and Jos H F F 1990 *J. Appl. Phys.* **68** 6191

Demaree J D, Kirkpatrick S R, Kirkpatrick A R and Hirvonen J K 1997 *Nucl. Instrum. Methods Phys. Res. B* **127/128** 603

Diaz de la Rubia T, Averback R S, Benedek R and Robertson I M 1990 *Radiat. Eff. Defects Solids* **113** 39

Diens G J and Damask A C 1958 *J. Appl. Phys.* **29** 1713

Eaglesham D J, Stolk P A, Gossman H J and Poate J M 1994 *Appl. Phys. Lett.* **65** 2305

Fielitz P, Macht M P, Naundorf V and Wollenberger H 1997 *J. Nucl. Mater.* **251** 123

Kapinos V G and Platonov P A 1985a *Phys. Status Solidi a* **90** 291

Kapinos V G and Platonov P A 1985b *Phys. Status Solidi a* **91** K9

Kapinos V G and Platonov P A 1987 *Radiat. Eff.* **103** 45

Lee Y S, Averback R S and Flynn C P 1994 *Phil. Mag. Lett.* **70** 269

Lof P 1987 *Elsevier's Periodic Table of The Elements* (Amsterdam: Elsevier Science)

Lu M, Lupu C, Lee S M and Rabalais J W 2001 *J. Chem. Phys.* **115** 446

Lu M, Lupu C, Styve S J, Lee S M and Rabalais J W 2002a *J. Vac. Sci. Technol. A* **20** 174

Lu M, Lupu C, Lee S M and Rabalais J W 2002b *J. Vac. Sci. Technol. A* **20** 180

Lu M, Lupu C and Rabalais J W 2002c *J. Appl. Phys.* **92** 3591

Lu M, Lupu C and Rabalais J W 2002d *Appl. Phys. Lett.* **81** 5033

Lu M, Lupu C, Lee S M and Rabalais J W 2002e *J. Vac. Sci. Technol. A* **21** 359

Lu M, Lupu C and Rabalais J W 2003 *J. Chem. Phys.* **118** 1433

Lupu C 2003 *PhD Dissertation* University of Houston

Macht M P and Naundorf V 1982 *J. Appl. Phys.* **53** 7551

Mackrodt W C and Stewart R F 1977 *J. Phys. C: Solid State Phys.* **10** 1431

McHargue C J 1998 *SPIE* **3413** 65

McHargue C J and Snyder W B Jr 1983 *SPIE* **2018** 135

Moller K, Jones K S and Law M E 1998 *Appl. Phys. Lett.* **72** 2547

Moya E G, Moya F, Bigarre J, Juve D, Treheux D and Grattepain C 1998 *Mater. Res. Soc. Symp.* **527** 533

Mrowec S 1980 *Defects and Diffusion in Soilds, An Introduction* (Amsterdam: Elsevier)

Mueller A, Naundorf V and Macht M P 1988 *J. Appl. Phys.* **64** 3445

Nordlund K and Averback R S 1997 *Appl. Phys. Lett.* **70** 3101

Ohkubo M, Hioki T and Kawamoto J 1986 *J. Appl. Phys.* **60** 1325

Pang T 1997 *An Introduction to Computational Physics* (New York: Cambridge University Press)

Partyka P, Zhong Y, Nordlund K, Averback R S, Robinson I M and Ehrhart P 2001 *Phys. Rev. B* **64** 235207

Perry S S and Merrill P B 1997 *Surf. Sci.* **383** 268

Pramanik D and Seidman D N 1983 *Nucl. Instrum. Methods Phys. Res.* **209/210** 453

Rafferty C S, Gilmer G H, Jaraiz M, Eaglesham D and Gossman H J 1996 *Appl. Phys. Lett.* **68** 2395

Sangster M J L and Stoneham A M 1984 *J. Phys.: Condens. Matter* **17** 6093

Shao L, Lu X, Jin J, Li Q, Liu J, van der Heide P and Chu W K 2000 *Appl. Phys. Lett.* **76** 3953

Sizmann R 1978 *J. Nucl. Mater.* **69/70** 386

Specht E D, Sparks C J and McHargue C J 1992 *Appl. Phys. Lett.* **60** 2216

Van Sambeek A I, Averback R S, Flynn C P, Yang M H and Jaeger W 1998 *J. Appl. Phys.* **83** 7576

Weast R C (ed) 1995 *CRC Handbook of Chemistry and Physics* (Boca Raton, FL: CRC Press)

Wei L C, Lang E, Flynn C P and Averback R S 1999 *Appl. Phys. Lett.* **75** 805  
Weiss M, Lu M, van der Heide P, Lee S M, Ada E T, Lee H and Rabalais J W 2000 *J. Chem. Phys.* **113** 5058  
Wen J M, Evans J W, Bartelt M C, Burnett J W and Thiel P A 1996 *Phys. Rev. Lett.* **76** 652  
Yang M H and Flynn C P 1994 *Phys. Rev. Lett.* **73** 1809  
Zhou Q and Manasreh M O 2002 *Appl. Phys. Lett.* **80** 2072  
Ziegler J F (ed) 1996 *The Stopping and Range of Ions in Solids* (New York: Pergamon)  
Zinkle S J and Kinoshita C 1997 *J. Nucl. Mater.* **251** 200